nature sustainability

Article https://doi.org/10.1038/s41893-026-01787-x

Rewiring energy flow in biohybrids for enhanced solar-driven biosynthesis

Received: 4 August 2025

Accepted: 5 February 2026

Mingming Guo[1,2,9], Xinke Kong[3,9], Xin Wang[1], Wenbo Cheng[2,4], Hu Li[5], Hui Xia[5], Wenjun Yang[1], Yang Xiang[1], Shanshan Pi[1,6], Rui Ma[7], Yiliang Lin[8], Chen Yang[5] ✉, Yuanyuan Wang[3] ✉ & Xiang Gao[1] ✉

Semiconductor biohybrids offer a viable approach to harness solar energy for the biosynthesis of high-value energy-rich long-chain compounds (ERLCCs). However, solar-driven ERLCC biosynthesis routes are often hindered by the inefficient conversion of light energy into cytosolic cofactors. Here we present a design strategy to rewire energy flow in biohybrids, enabling efficient solar-to-ERLCC conversion. Specifically, by tuning the morphology and structure of semiconductors we constructed an intracellular biointerface within engineered heterotrophic *Vibrio natriegens* chassis. This CdS–*V. natriegens* biohybrid achieved a solar-to-2,3-butanediol (BDO) conversion efficiency of 2.35%. Multi-omics and biochemical analyses identified an electron mediator, thiamine pyrophosphate, exogenous supplementation of which enhanced cofactor regeneration, further increased the solar-to-BDO efficiency to 2.83% and achieved a carbon yield of 0.497 g g^{-1}. This biohybrid platform was further extended to produce polyhydroxybutyrate and α-farnesene, and upcycle various waste-carbon sources—including mannitol, cellulose, chitosan and industrial wastewater—into BDO. In a 5-l fed-batch bioreactor using wastewater as the sole carbon source, the system achieved a BDO titre of 30.71 g l^{-1}, demonstrating its scalability and robustness. This study establishes a versatile framework for solar-driven microbial biomanufacturing and waste-to-value conversion, paving the way to carbon-efficient chemical production.

Solar-driven microbial biomanufacturing holds great promise for sustainable chemical production with enhanced carbon and energy efficiency[1,2]. Biohybrid systems, which integrate light-harvesting semiconductors with the metabolic versatility of living cells, have emerged as a powerful platform for solar-to-chemical conversion[3,4]. To date, efforts have largely focused on autotrophic bacterial hybrids for the production of simple molecules such as hydrogen and acetate[5,6]. However, the limited availability of genetic tools for these strains has constrained their ability to synthesize more complex or diverse products[7]. In contrast, heterotrophic microorganisms offer extensive genetic toolkits and robust biosynthetic capabilities, making them ideal chassis for the production of a wide range of industrial chemicals, including energy-rich long-chain compounds (ERLCCs)[8,9]. Recent advances in heterotrophic biohybrid systems have demonstrated the potential to couple solar energy with intracellular regeneration of key energy cofactors—namely, reduced nicotinamide adenine dinucleotide (NADH) and adenosine triphosphate (ATP)—to drive value-added biosynthetic pathways[10–12]. A cost-effective and sustainable large-scale biosynthesis of semiconductor biohybrids approach was recently developed[12]. Despite this progress, current systems face substantial limitations in converting solar energy into intracellular energy cofactors with sufficient efficiency to support ERLCC biosynthesis[13]. As a result, the reported solar-to-ERLCC conversion efficiencies remain substantially lower than those achieved for simple molecules, and their application

---

A full list of affiliations appears at the end of the paper. ✉e-mail: yang.c@sjtu.edu.cn; wangyy@nju.edu.cn; gaoxiang@siat.ac.cn

for producing ERLCCs from renewable carbon sources have not been well explored[14].

Solar-to-chemical conversion in biohybrid systems proceeds through three sequential steps: (1) generation and transfer of photoexcited electrons at the semiconductor–microbe interface; (2) intracellular regeneration of energy cofactors (NAD(P)H and ATP) driven by these electrons; and (3) cofactor-dependent biosynthesis of target chemicals[15]. Despite recent progress, each of these steps remains suboptimal in current biohybrid platforms[13,15]. First, the conversion of photons into biologically accessible electrons is often inefficient, due to rapid electron–hole recombination in the semiconductor and substantial energy loss during electron transfer across the insulating microbial membrane[16,17]. Second, the intracellular conversion of photoelectrons into energy cofactors is poorly understood and inefficient, representing a major bottleneck in driving downstream biosynthetic pathways[18,19]. Third, the use of solar energy to convert renewable or waste-derived carbon sources into ERLCCs remains largely unexplored[12]. Overcoming these limitations in an integrated manner is essential to unlock the full potential of solar-powered biomanufacturing and to establish heterotrophic microbial biohybrids as a high-efficiency platform for sustainable ERLCC production.

Here we developed a heterotrophic semiconductor–microbe biohybrid platform to enhance solar-to-chemical conversion efficiency for the production of ERLCCs (Fig. 1). By engineering semiconductor morphology and exploring intracellular electron mediation, we aimed to overcome key bottlenecks in light-driven cofactor regeneration and carbon yield, enabling scalable and sustainable biomanufacturing from diverse waste-carbon sources. This work presents a generalizable strategy for converting solar energy and low-cost waste carbon into value-added chemicals.

Results

Engineering biohybrid interfaces for electron utilization

The material–microbe interface is pivotal to photoelectron generation and transfer in semiconductor biohybrids[13,20]. Internalized nanomaterials can establish intracellular biointerfaces that bypass cross-membrane energy loss, thus facilitating photoexcited electron delivery to the cytosol[15,21,22]. We synthesized low-dimensional nanomaterials[16], including zero-dimensional (0D) nanoparticles or quantum dots, 1D nanotubes or nanorods and 2D nanosheets or nanoplatelets (NPLs)[23–25] (Fig. 2a), characterized their morphologies and properties, then analysed their internalization rates in bacteria. Surprisingly, all materials were internalized rapidly by bacteria, and 2D NPLs exhibited the highest uptake rate (Supplementary Discussion 1). This is probably attributed to their flat, ultra-thin structure and adaptability to bacterial surface topographies[26,27].

We next designed the structure of 2D NPLs to improve the electron generation at the intracellular biointerface. The thickness of 2D NPLs has been reported to modulate carrier kinetics during the charge separation process. In addition to 4-monolayer (ML) NPLs, we then synthesized thicker (5 ML) and thinner (3 ML) NPLs, and assessed the photoelectrical efficiency of those nanomaterials. As details in Supplementary Discussion 2, 5-ML NPLs exhibited superior photoelectric conversion efficiency. To further improve charge separation, we engineered a type-II CdS/ZnSe NPL core–crown (CC) heterostructure[28,29]. ZnSe was chosen for its narrow bandgap to tune the energy levels of the CdS core[30]. Transmission electron microscopy (TEM) imaging revealed rectangular NPLs (45 × 45 × 2.2 nm), and energy-dispersive spectroscopy (EDS) mapping confirmed the spatial separation of the CdS core and ZnSe crown (Fig. 2b and Supplementary Fig. 10a). Raman spectra showed a Cd–S bond signal at ~302 cm^{-1}, while X-ray diffraction confirmed the zinc blende crystal structure (Fig. 2c,d). CC NPLs displayed the strongest absorption at 440 nm, emission at 510 nm (Fig. 2f), and achieved the highest photocurrent output (2.63 $\mu\text{A cm}^{-2}$), a 1.445-fold improvement over 5-ML NPLs (1.82 $\mu\text{A cm}^{-2}$; Fig. 2e and Supplementary Fig. 9), while their cellular internalization rate (46.14 $\text{mg l}^{-1}\text{ h}^{-1}$) was comparable to that of 5-ML NPLs (48.45 $\text{mg l}^{-1}\text{ h}^{-1}$; Supplementary Fig. 4). The results indicate that increasing the thickness of 2D materials enhances charge separation and photoactivity by narrowing the bandgap and improving electron mobility, while the CC NPLs further boost charge separation efficiency.

We then evaluated the solar-to-chemical conversion efficiency using a 2,3-butanediol (BDO)-producing *Vibrio natriegens* strain (XG211), constructed by introducing the pET28a-*RABC* plasmid[31] encoding the BDO biosynthetic pathway. Because the bioproduction of BDO is dependent on the supply of energy cofactors, it serves as an excellent platform for evaluating the energy efficiency of biohybrids. We added the nanomaterials (1.5 mg l^{-1}, identified as the optimal concentration under tested conditions) to the cell suspension ($\text{OD}_{600} \approx 2.0$, optical density at 600 nm) of strain XG211 in the minimum medium with 4 g l^{-1} glucose, electron sacrificial agent (cysteine) and mediator (flavin mononucleotide (FMN)), the most effective mediator under tested conditions (Supplementary Figs. 13 and 14). The CC NPLs–XG211 system under illumination outperformed all configurations, producing 1.68 g l^{-1} BDO—2.65 times higher than bacteria alone (0.63 g l^{-1}) and 1.9 times higher than dark conditions (0.87 g l^{-1}) (Fig. 2g and Supplementary Discussion 3). We subsequently assessed the carbon yield of bacteria and biohybrids, finding that the CC NPLs biohybrids exhibited the highest carbon yield, reaching 0.457 g g^{-1}, and this value is 2.69 times higher than that of bacteria alone and represents a 1.98-fold increase compared with dark conditions (Fig. 2h and Supplementary Fig. 16b). Furthermore, the solar-to-chemical efficiency of the CC NPLs–XG211 biohybrid was 2.35%, which was 7.83-fold than that of quantum dots–XG211 (0.3%) (Supplementary Fig. 32). This indicates that the high BDO titre was not owing to rapid glucose consumption, but rather to photoexcited electrons generated by the material and transferred to the bacteria, thereby enhancing BDO biosynthesis.

We further investigated the biointerface and charge-transfer kinetics of this best biohybrid system. We first prepared cross-sectional slices of CC NPLs–XG211 biohybrid samples using a microtome. High-angle angular dark-field scanning transmission electron microscopy (HAADF-STEM) image and EDS mapping showed that internalized CC NPLs were composed of Cd, S, Zn and Se, with highly correlated locations (Fig. 2i and Supplementary Fig. 10). Those results clearly revealed the successful transportation of CC NPLs into the cytoplasm of *V. natriegens*, contributing to an enhanced efficiency of photoelectron transfer and energy transduction[32]. We then studied the charge-transfer kinetics through the photoexcited electron lifetime and photocurrent of both CC NPLs–XG211 biohybrids and pure CC NPLs (Fig. 2j). The average photogenerated state lifetime of biohybrids was only 0.26 ± 0.01 ns (mean ± s.d.), showing a 280-fold reduction compared with the CC NPLs alone (72.8 ± 5.2 ns, mean ± s.d.; Fig. 2k). To gain insight into the photoinduced charge-transfer dynamics within the biohybrid system, transient absorption spectroscopy was conducted. Upon photoexcitation, CC NPLs (monitored at 470 nm) exhibited a very rapid normalized bleach decay within 300 ps, indicative of ultrafast electron–hole separation. When integrated with XG211, the decay dynamics became faster within the first 50 ps, followed by a slower decay beyond 100 ps. Such changes in transient kinetics are characteristic signatures of ultrafast charge transfer (Fig. 2l). Similarly, upon the addition of bacteria, the photocurrent of biohybrid systems decreased by about 69.96% compared with that of CC NPLs alone (Supplementary Fig. 17). Moreover, without the electron donor (cysteine), the BDO production of the illuminated biohybrids was similar to the bacteria alone. Upon cysteine supplementation, BDO titre and carbon yield of the biohybrids both increased 2.45-fold compared with the bacterial control, underscoring the necessity of external electron donors (Fig. 2m,n). Collectively, these results demonstrate that intracellular assembly of CC NPLs facilitates rapid photogenerated charge separation and delivery into microbial metabolism, thus boosting solar-to-chemical conversion efficiency.

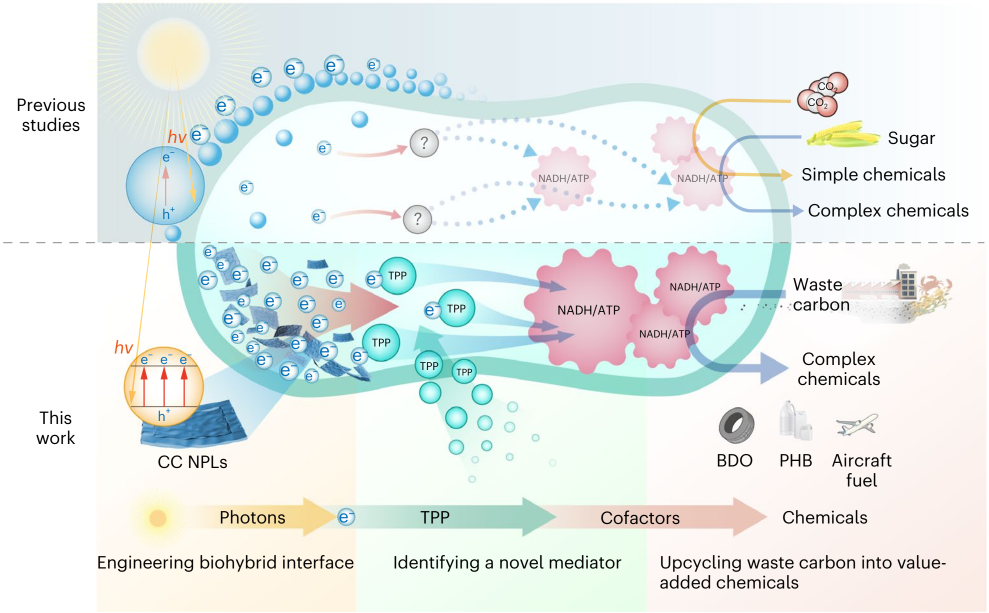

Fig. 1 | Rewiring energy flow in semiconductor–microbe biohybrids for solar-driven waste valorization. Schematic overview comparing previous biohybrid approaches with this work. Prior systems showed limited electron delivery due to poor cellular uptake of semiconductors and unclear intracellular electron utilization, often relying on CO$_2$ or sugars for simple molecule synthesis. In contrast, our strategy combines the following: (1) structured NPLs for enhanced internalization and electron transfer; (2) TPP-mediated cofactor regeneration; and (3) broad feedstock compatibility for efficient production of ERLCCs from diverse waste-carbon sources. *hv*, incident photon; e$^-$, reducing equivalent; h$^+$, hole.

Thiamine pyrophosphate mediates photoelectron-driven cofactor regeneration

To investigate how intracellular photoelectrons convert into energy cofactors (NAD(P)H and ATP)—a largely unknown process[15]—we conducted benchmark experiments to analyse the changes of energy cofactors, including the NAD(P)H/NAD(P)$^+$ ratio, which indicated the redox energy state of cells and ATP/ADP ratio concentration. At 0 h, the NADH/NAD$^+$ and NADPH/NADP$^+$ ratios were similar across all groups. However, after 0.5 h and 1 h of illumination, the NADH/NAD$^+$ ratios in the biohybrid increased notably, reaching values of 0.45 and 0.83, respectively, representing a 72.68% and 1.02-fold increase relative to the dark conditions (Fig. 3a). Similarly, the NADPH/NADP$^+$ ratio under illumination increased by 18.2% and 27.41% compared with the dark control, and by 10.77% and 26.09% relative to the bacteria alone (Fig. 3a). Consistently, the results obtained using the NADH/NAD$^+$ and NAD(P)H/NAD(P)$^+$ sensors, which monitor the real-time dynamic changes of the in vivo redox state, exhibited similar trends (Supplementary Discussion 4). Concurrently, the intracellular ATP/ADP ratio in illuminated biohybrids increased by 11.35% and 25.39% at 0.5 h and 1 h, respectively, compared with the dark conditions, and were 5.93% and 24.8% higher than those in control bacteria alone (Fig. 3b). These results indicate that the CC NPLs biohybrids rewire solar energy for the regeneration of extra-energy cofactors besides the intricate sugar oxidation, which typically releases CO$_2$ and has a lower glucose-to-chemical carbon yield[33]. These results are consistent with the above results, indicating that the carbon yield of CC NPLs biohybrids was higher than that of the bacteria alone under illumination (Fig. 2h).

We next performed metabolomics and transcriptomics to dissect regulation of intracellular CC NPLs on bacterial metabolism. We collected biohybrid samples under light and dark conditions for targeted metabolite quantification using liquid chromatography–tandem mass spectrometry (LC–MS/MS). Central metabolic pathways such as glycolysis, the tricarboxylic acid cycle and the pentose phosphate pathway, the native sources of energy cofactors and precursors for product biosynthesis, were analysed. As shown in Fig. 3c, the intracellular concentration of key metabolites such as glucose-6-phosphate, fructose-1,6-bisphosphate, 3-phosphoglycerate and phosphoenolpyruvate in the glycolysis, as well as acetyl-coenzyme A and malate in the tricarboxylic acid cycle, were increased under light compared with dark conditions. The concentration of 6-phosphogluconate in the pentose phosphate pathway was also higher under light than dark conditions (Fig. 3c). Additionally, acetoin, a biosynthetic precursor of BDO, exhibited a 96.8% increase in production under illumination than dark condition (Supplementary Fig. 20). Together, these metabolic shifts suggest that nanomaterial-induced photoelectrons enhance central carbon metabolism, consistent with previous findings in similar systems[12,34].

To further elucidate how CC NPLs influence cellular regulation at the transcriptional level, we performed RNA sequencing (RNA-seq) analysis comparing gene expression profiles of biohybrids under light and dark conditions. This analysis revealed 22 notably upregulated and 8 downregulated genes under illumination, using a stringent cutoff of $|\log_2(\text{fold change})| > 1.5$ and $P < 0.01$ (Fig. 3d,e). As shown in Fig. 3d,e, the upregulated genes include those encoding proteins involved in cellular energy metabolism with illumination, such as the oxidative respiratory chain (complex Ⅰ (NADH-quinone reductase), complex Ⅱ (fumarate reductase), complex Ⅳ (cytochrome ubiquinol oxidase)), FAD (flavin adenine dinucleotide, FMN transferase) and RNF (ferredoxin: NAD$^+$ oxidoreductase complex, electron transport complex), as well as the ATPase (ATP synthase). Remarkably, 7 out of 22 upregulated genes were involved in thiamine biosynthesis, suggesting an unexpected role for thiamine pyrophosphate (TPP)—the biologically active form of thiamine—in light-driven metabolism (Supplementary Discussion 5).

Given these findings, we hypothesized that TPP may act as a redox mediator that facilitates the transfer of photoelectrons to cofactor regeneration pathways. To test this hypothesis, we conducted in vitro NADH regeneration assays using purified CC NPLs (Fig. 3f). In a typical experiment, 1.5 mg ml^{-1} CC NPLs with 1 mM NAD$^+$ and TPP were inoculated under 470-nm light (5 mW cm^{-2}), the control without TPP addition was also included. NADH regeneration was monitored by the

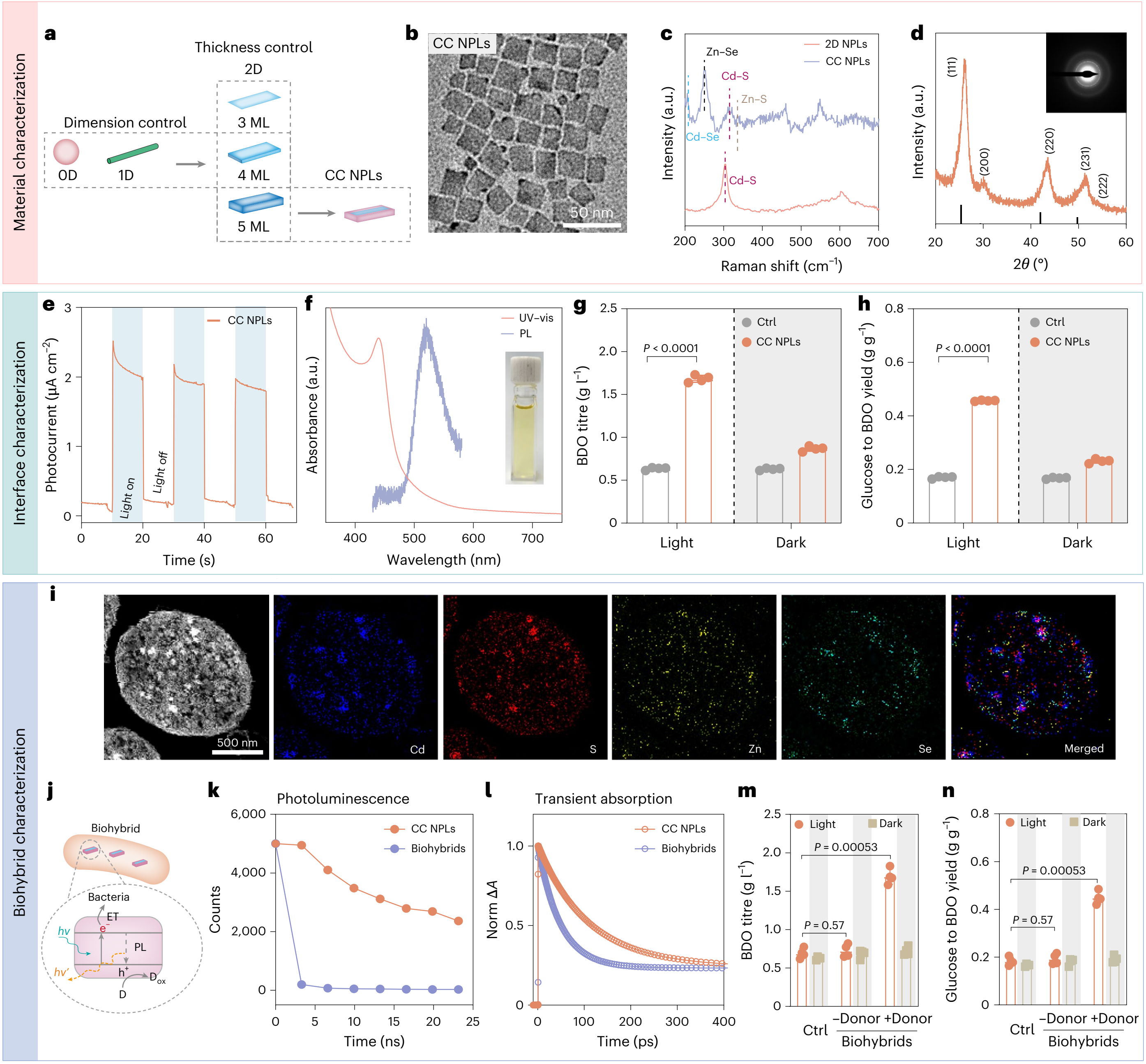

Fig. 2 | Design of biohybrid interfaces and characterization of biohybrid system performance. a, The rational design of semiconductors based on their varied dimensions and charge separation. **b**, TEM images of CC NPL semiconductors. **c**, Raman spectrum of 2D NPLs (bottom trace) and CC NPLs (upper trace). **d**, X-ray diffraction pattern of CC NPLs. **e**, Photocurrent response in CC NPLs (470 nm, 5 mW cm^{-2}). Materials concentration: 1.5 mg l^{-1}. **f**, UV–vis absorbance and photoluminescence (PL) emission spectra of CC NPLs (with sample photograph insert). **g**, BDO titre of bacteria and CC NPLs–XG211 biohybrids under light (470 nm, 5 mW cm^{-2}) and dark. **h**, Glucose to BDO yield of bacteria and CC NPL semiconductors-BDO biohybrid systems under light and dark. **i**, HAADF-STEM image and EDS mapping of the CC NPLs–XG211 biohybrid systems, showing the distribution of key elements and the material–bacteria interface. **j**, Schematic illustration of the CC NPLs–XG211 biohybrids interface (not drawn to scale). ET, electron transfer; D, cysteine; D$_{ox}$, cystine. **k**, Time profiles of normalized transient absorption and the lifetime of biohybrids' photoexcited states as determined by time-correlated single-photon counting. **l**, Transient kinetics for pure CC NPLs and CC NPLs–XG211 biohybrids. Norm Δ*A* denotes the transient absorption change (Δ*A*) normalized to its maximum. **m**,**n**, The BDO titre (**m**) and carbon yield (**n**) of the biohybrids with and without the addition of electron donors (cysteine) in both light (470 nm, 5 mW cm^{-2}) and dark conditions. For **g**, **h**, **m** and **n**, the data are presented as the mean ± s.d. from 4 independent measurements ($n = 4$). All *P* values are determined by a two-tailed unpaired *t*-test.

absorption at 340 nm (Abs 340 nm) and the final NADH product was confirmed by nuclear magnetic resonance (NMR; Fig. 3g). Adding TPP resulted in a 4.45-fold increase in NADH production under light conditions compared with controls without TPP, whereas NADH production remained unchanged under dark conditions (Fig. 3h). In contrast, TPP alone did not promote NADH regeneration under either light or dark conditions (Fig. 3h). These findings were corroborated by NMR, affirming that the increase in Abs 340 nm was indeed attributable to heightened NADH production (Fig. 3g). Similarly, supplementation with thiamine (vitamin B$_1$)—a precursor of TPP—also boosted NADH production 9.45-fold under light, with nearly all of the produced active 1,4-NADH, while no effect was observed in the dark (Fig. 3i and Supplementary Discussion 6). In contrast, the addition of thiamine alone did not promote NADH regeneration under either light or dark conditions

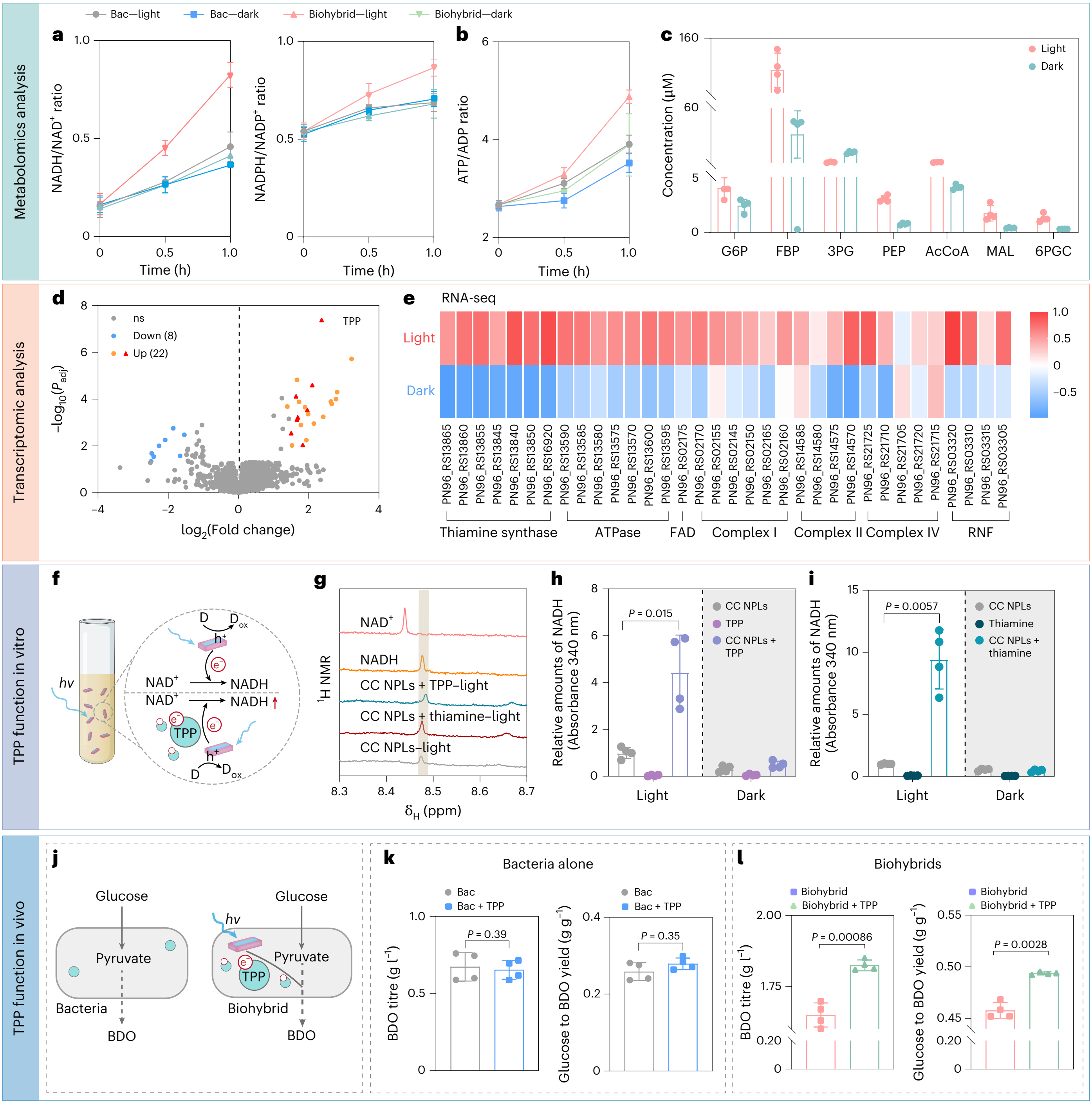

Fig. 3 | Metabolites and gene expression analysis in photocatalytic biohybrids. **a**, The NADH/NAD$^+$ and NADPH/NADP$^+$ ratios at multiple time points (0 h, 0.5 h and 1 h) after the initial reaction in bacteria (Bac) XG211 and the biohybrids were measured under illumination (5 mW cm^{-2}) and dark conditions. **b**, The ATP/ADP ratio of XG211 and the biohybrid were measured at 0 h, 0.5 h and 1 h under both illuminated (5 mW cm^{-2}) and dark conditions to evaluate light-responsive energy generation. **c**, Intracellular metabolite concentrations in CC NPLs–XG211 biohybrids under light (5 mW cm^{-2}) and dark. G6P, glucose-6-phosphate; FBP, fructose-1,6-bisphosphate; 3PG, 3-phosphoglycerate; PEP, phosphoenolpyruvate; AcCoA, acetyl-coenzyme A; MAL, malate; 6PGC, 6-phosphogluconate. **d**, Volcano plot revealing differentially expressed genes in biohybrids under light and dark conditions, showing upregulated and downregulated genes. Blue: genes downregulated under light relative to dark conditions. Orange and red: genes downregulated under light relative to dark conditions (the red triangles represent genes related to thiamine synthesis); grey: non-significant (ns) genes; the number of regulated genes are indicated in brackets. **e**, Heatmaps showing significantly regulated genes from RNA-seq analysis, with colour intensity indicating relative expression levels across different samples or treatments. **f**, Schematic diagram illustrating the TPP- or thiamine-mediated conversion of photoelectrons into energy cofactors in vitro. **g**, NMR analysis was conducted under in vitro photonic conditions with the addition of TPP or thiamine and CC NPLs catalysing the conversion of NAD$^+$ to NADH. **h**, NADH regeneration under light (470 nm, 5 mW cm^{-2}) and dark conditions for TPP alone, CC NPLs alone and CC NPLs supplemented with TPP. **i**, NADH regeneration under light (470 nm, 5 mW cm^{-2}) and dark conditions for thiamine alone, CC NPLs alone and CC NPLs supplemented with thiamine. **j**, Schematic illustration of intracellular electron transfer in bacteria and biohybrids supplemented with TPP. **k**, BDO titre and carbon yield of bacteria alone under light conditions, with and without TPP supplementation. **l**, BDO titre and carbon yield of monocultured bacteria and biohybrids, with or without TPP, under light conditions. For **a**–**c**, **h**, **i**, **k** and **l**, the data are presented as the mean ± s.d. from 4 independent measurements ($n = 4$). All *P* values are determined by a two-tailed unpaired *t*-test.

(Fig. 3i). The photoelectrochemical analysis further confirmed that TPP is capable of accepting electrons derived from the CC NPLs (Supplementary Discussion 6). Based on these results and corresponding in vitro experiments, both TPP and thiamine not only enhance reducing power production from photoelectrons but also boost the native central metabolism. Recent studies also suggest that TPP/thiamine promotes NADH production and electron transfer in two bacterial species co-cultures[35]. We speculated that TPP might mediate the conversion of intracellular photoelectrons into energy cofactors (NAD(P)H and ATP), and thus enhance solar-to-chemical efficiency in the biohybrids.

To test this hypothesis, we evaluated BDO titre and carbon yield in both bacterial and biohybrid systems with and without TPP supplementation (Fig. 3j). In the bacterial system without nanomaterials, TPP addition had no significant effect on either BDO titre or carbon yield, indicating that TPP alone does not enhance biosynthesis in the absence of photoelectrons (Fig. 3k). In contrast, in the CC NPLs-based biohybrid system, TPP supplementation under illumination increased BDO titre by 10.63% and carbon yield by 7.84% compared with the unsupplemented conditions (Fig. 3l). In addition, we confirmed that TPP functions as a mediator receiving electrons from CC NPLs, rather than serving as a cofactor via benchmark control experiments including (±FMN, ±TPP, ±cysteine, ±light; Supplementary Discussion 7).

To investigate further, we cultured biohybrid systems with varying concentrations (0, 0.3, 0.6, 1, 3, 6 mM) of TPP or thiamine. As detailed in Supplementary Discussion 7, 0.6 mM TPP supplementation resulted in the highest BDO production and carbon yield. At this optimal concentration, TPP significantly enhanced the performance of the biohybrid system under illumination, achieving a solar-to-chemical conversion efficiency of 2.83% and the highest reported carbon yield (0.497 g g^{-1}; Supplementary Fig. 15 and Supplementary Table 4). Notably, higher TPP levels favoured biomass accumulation rather than product synthesis. These findings indicate that TPP functions not as a biosynthetic cofactor, but as an effective electron mediator that facilitates more efficient photogenerated electron transfer for chemical production. Metabolic flux analysis using the *V. natriegens* genome-scale model iLC858 (Supplementary Discussion 8) further indicated that TPP-enhanced NADH regeneration redirected reducing power from the by-product pathway towards BDO synthesis, thereby increasing both production flux and carbon efficiency. Next, we sought to determine whether other cellular systems contribute to photoelectron transduction. Given that oxidative phosphorylation is essential for energy conservation and has previously been implicated in extracellular electron transfer, we investigated the role of the respiratory chain in photoelectron conversion[34]. The upregulated genes in Fig. 3e, such as encoding complex Ⅰ, complex Ⅱ, complex Ⅳ, ATPase, FAD and RNF, were chosen as target inhibited genes using single guide RNA. CRISPR interference (CRISPRi) analysis verified the critical role of the oxidative respiratory chain in electron transfer (Supplementary Discussion 9).

Taken together, we found that TPP mediated the conversion of intracellular photoelectrons into the energy cofactor, and the materials-induced photoelectrons regulated both carbon metabolism and energy metabolism of bacteria, rewiring the solar energy into chemicals. Based on the understanding of the regulation mechanism of the pivotal steps of energy flows further guides the design of biohybrid systems for more efficient solar-to-chemical production with higher carbon yield.

A light-driven biohybrid platform for waste-carbon upgrading

To demonstrate the versatility of our biohybrid system, we extended its application beyond BDO to the production of other ERLCCs, including polyhydroxybutyrate (PHB) and α-farnesene. PHB is a biodegradable biopolymer that presents a sustainable alternative to petroleum-derived plastics[34]. To construct a PHB-producing strain, we introduced the PHB biosynthetic plasmid pET28a-*phaCAB*[36] into *V. natriegens*, generating strain XG256 (Fig. 4a and Supplementary Fig. 43). As shown in Fig. 4a–d, using a similar design, the CC NPLs-based biohybrid system with TPP under illumination was superior to all other conditions. The resulting PHB content, productivity and production yield were 0.95 g gCDW^{-1} (cell dry weight), 1.27 g l^{-1} h^{-1} and 0.392 g g^{-1}, respectively, representing increases of 1.73-fold, 2.13-fold and 2.1-fold compared with the bacterial control. Notably, both the PHB content (g gCDW^{-1}) and the carbon yield from glucose to PHB were higher than those previously reported in industrial microorganisms to date (Supplementary Fig. 44 and Supplementary Table 2).

We next validated the platform's ability to produce α-farnesene, a sesquiterpene hydrocarbon that can be hydrogenated to generate farnesane—a renewable drop-in diesel and aviation fuel with excellent cold-weather performance and high energy density[37]. To synthesize α-farnesene, we constructed strain XG257 by incorporating the α-farnesene biosynthetic pathway expressed from two plasmids, Keasling2187[38] and pFZ71[39] (Fig. 4e and Supplementary Fig. 45), into *V. natriegens*. As with PHB, the CC NPLs–TPP biohybrid system under illumination substantially outperformed all control conditions (Fig. 4e–h). Notably, the glucose-to-α-farnesene carbon yield reached 78.95 mg g^{-1}, representing a higher level among current industrial microorganisms (Supplementary Fig. 46 and Supplementary Table 3). These results underscore the broad applicability of the developed biohybrid system for high-efficiency solar-to-chemical conversion across diverse ERLCCs.

Subsequently, we evaluated the capability of the engineered biohybrids to directly convert waste-carbon source for producing ERLCCs. We employed the engineered BDO-producing strain XG211 and assessed performance using four representative waste feedstocks: mannitol (derived from brown algae waste), cellulose hydrolysate (from agricultural straw), chitosan hydrolysate (from crab shell waste) and molasses-based industrial wastewater (Fig. 5a). In all cases, the biohybrid system supported robust growth and light-driven BDO production, yielding titres of 0.51 g l^{-1} (mannitol), 1.67 g l^{-1} (cellulose hydrolysate), 0.38 g l^{-1} (chitosan hydrolysate) and 5.59 g l^{-1} (industrial wastewater). We further quantified carbon yields by calculating the amount of BDO produced relative to carbon source consumption (Fig. 5b–g). Among all substrates, molasses wastewater achieved the highest carbon yield at 0.18 g g^{-1}, which was 2.25-fold higher than that from mannitol (0.079 g g^{-1}), 1.04-fold higher than cellulose hydrolysate (0.17 g g^{-1}) and 3.7-fold higher than chitosan hydrolysate (0.048 g g^{-1}). These results demonstrate the system's ability to efficiently utilize waste-derived carbon sources of varying chemical complexity and composition.

Together, these findings establish that our solar-driven semiconductor–microbe biohybrid platform is not only versatile in producing multiple classes of ERLCCs but also highly adaptable to unrefined, inexpensive waste-carbon feedstocks. This capability enables the dual benefits of reducing feedstock costs and improving environmental sustainability by upcycling waste streams into high-value products.

Scaling-up biohybrids for solar-driven chemical production

To evaluate the scalability and industrial relevance of this approach, we conducted both batch and fed-batch fermentations in a 5-l bioreactor using molasses-based industrial wastewater as the sole carbon source (Fig. 5h and Supplementary Fig. 47). The biohybrid system successfully assimilated 73.44% of the sugars present in wastewater, supporting cell growth and BDO biosynthesis, and achieved a maximum cell biomass of 7.02 (Fig. 5i). Notably, the highest BDO titre and yield reached 30.71 g l^{-1} and 0.766 g g^{-1}, respectively (Fig. 5j). Excessively high cell density can hinder light penetration during fermentation, a challenge that can be mitigated through optimized stirring and bioreactor design (Supplementary Discussion 10). These results highlight the platform's robustness, scalability and adaptability to low-cost and complex feedstocks. Moreover, the use of industrial wastewater as the sole feedstock illustrates a pathway towards circular bioeconomy solutions, wherein waste streams are directly converted into high-value chemicals, thereby reducing environmental impacts while improving economic feasibility.

To comprehensively evaluate the environmental and economic advantages of our system, we conducted a life-cycle assessment (LCA),

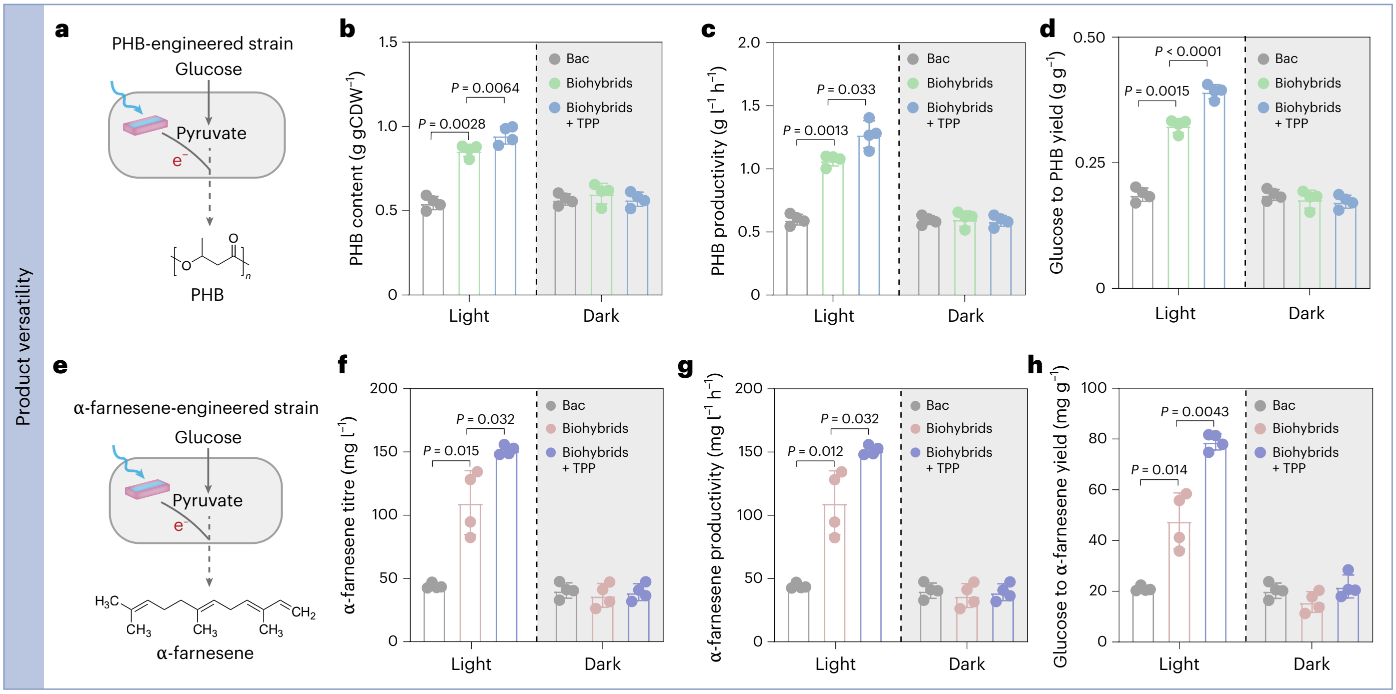

Fig. 4 | Scalability of products of biohybrid systems. **a**, Schematic illustration of a biohybrid system engineered to overexpress the *phaCAB* gene cluster for the biosynthesis of PHB. **b**, PHB content of bacteria, biohybrids and TPP-supplemented biohybrids under light and dark conditions. **c**, PHB productivity of bacteria, biohybrids and TPP-supplemented biohybrids under light and dark conditions. **d**, Glucose to PHB yield of bacteria, biohybrids and TPP-supplemented biohybrids under light and dark conditions. **e**, Schematic illustration of a biohybrid system engineered to overexpress the α-farnesene synthetic pathway for the biosynthesis of α-farnesene. **f**, α-farnesene titre of bacteria, biohybrids and TPP-supplemented biohybrids under light and dark conditions. **g**, α-farnesene productivity of bacteria, biohybrids and TPP-supplemented biohybrids under light and dark conditions. **h**, Glucose to α-farnesene yield of bacteria, biohybrids and TPP-supplemented biohybrids under light and dark conditions. For **b**–**d** and **f**–**h**, the data are presented as the mean ± s.d. from 4 independent measurements ($n = 4$). All P values are determined by a two-tailed unpaired t-test.

benchmarking it against previously reported wastewater-derived biohybrid systems for BDO production[12] (Fig. 6a–e). Our analysis revealed several key improvements: reduced consumption of buffer solutions, and freshwater, coupled with a substantial increase in BDO titre (from 13.09 to 30.71 g l^{-1}). Contribution analysis of greenhouse gas (GHG) emissions and cost drivers for solar-driven biohybrid BDO production from wastewater revealed that the energy required for product separation from the cultivation system—primarily derived from natural gas—accounted for 27.46% of total GHG emissions and 25.47% of production costs (Fig. 6f,g). The buffer solution was identified as the primary cost driver, contributing 47.71% of total costs (Fig. 6f,g). Utilizing free wastewater as feedstock effectively decouples BDO production from fluctuations in commodity feedstock prices. Compared with the previously reported biohybrid system[12], our optimized platform significantly reduced both GHG emissions and production costs, achieving values of 0.30 ± 0.034 kg CO_2 equivalents (CO_2e) per kg BDO and US\$0.201 ± 0.037 per kg BDO, respectively—representing more than a 40% reduction in emissions and over a 90% reduction in cost (Fig. 6b–e, and Supplementary Tables 9 and 10). Furthermore, this biohybrid system demonstrated lower environmental impacts across multiple indicators, including resource depletion, terrestrial acidification and human health effect (Supplementary Tables 11 and 12, and Supplementary Discussion 10). These improvements can be attributed to the dual benefits of sustainable resource recovery and environmental remediation embedded within the biohybrid fermentation process. Future studies should include factors such as the electron–hole separation efficiency of materials, sacrificial agents and TPP, as these may influence the life-cycle impacts of BDO production via biohybrid fermentation. Continued investigation and system refinement will be essential to fully realize the industrial potential of wastewater-driven biomanufacturing.

Discussion

Biohybrid systems direct harvesting of solar energy for regenerating intracellular cofactors, thereby minimizing carbon loss and improving both productivity and carbon yield in biomanfucturing[34]. However, achieving efficient solar-to-cofactor conversion in heterotrophic microbes for ERLCC production remains challenging[13,40]. Here we establish a design framework for rewiring energy flow in heterotrophic semiconductor–microbe biohybrids, substantially advancing solar-driven biosynthesis of ERLCCs. By tuning semiconductor morphology and uncovering TPP as an intracellular redox mediator, we improved photogenerated cofactor regeneration and enabled high-yield production of target chemicals. These findings provide critical mechanistic insights into photoelectron utilization in microbial systems and contribute broadly to the fields of synthetic biology, microbial metabolism and solar-to-chemical energy conversion.

From a sustainability perspective, the developed platform illustrates the potential of combining solar energy with low-cost and waste-derived carbon substrates for biomanufacturing. The modularity of the system enables its extension to multiple ERLCCs and diverse feedstocks, including industrial waste streams, highlighting its relevance to circular bioeconomy concepts. By decoupling chemical production from refined sugars and fossil-derived inputs, such biohybrid strategies may contribute to reducing the environmental footprint of microbial manufacturing while expanding the scope of solar-to-chemical conversion technologies. Looking forward, the modularity of our platform suggests that more complex biosynthetic pathways—such as those requiring cytochrome P450s or iterative redox steps—could also be supported, opening opportunities for the solar-powered synthesis of value-added chemicals.

Despite these advances, several challenges remain. Scaling-up biohybrid systems will require light penetration limitations in dense

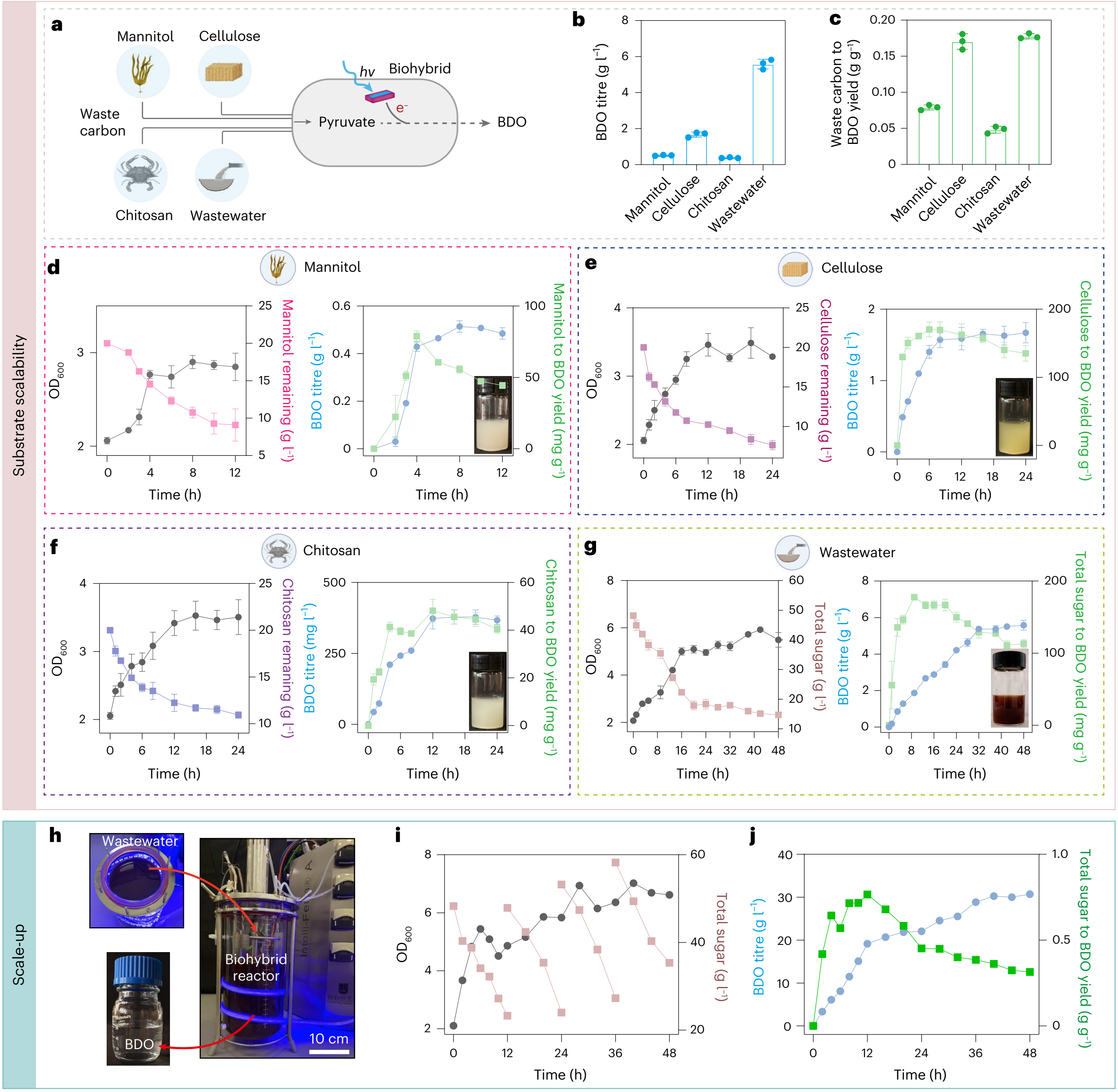

Fig. 5 | Scalability of substrates and scale-up of biohybrid systems. **a**, Schematic diagram illustrating a biohybrid system for the synthesis of value-added chemicals using waste carbon as the substrate. **b**,**c**, Maximum BDO titre (**b**) and carbon yield (**c**) of the biohybrid system using waste-derived carbon substrates. **d**–**g**, Bacterial growth, substrate consumption, BDO titre and carbon yield of the biohybrid system when utilizing mannitol (**d**), cellulose (**e**), chitosan (**f**) and wastewater (**g**) as substrates for BDO biosynthesis. **h**, Schematic representation of a 5-l fed-batch bioreactor for BDO titre by the biohybrid system using wastewater as the substrate. **i**, Growth curve and sugar consumption of the biohybrid system during fed-batch scale-up using wastewater from a single-run fermentation. **j**, BDO titre and carbon yield from total sugar to BDO during fed-batch scale-up of the biohybrid system with wastewater from a single-run fermentation. For **b**–**g**, the data are presented as the mean ± s.d. from 3 independent measurements ($n = 3$). All P values are determined by a two-tailed unpaired t-test. Illustrations in **a** and **d**–**g** created in BioRender; Guo, M. https://biorender.com/7c6h88h (2026).

cultures to be overcome, probably through integration with advanced photobioreactor designs. Further improvements in cost efficiency could be achieved by eliminating exogenous TPP supplementation, either by engineering endogenous overproduction or by introducing de novo TPP biosynthetic pathways. In addition, although cadmium-based semiconductors provide superior photophysical performance, transitioning to cadmium-free alternatives—such as zinc sulfide, zinc selenide, indium phosphide or carbon-based materials—will be essential for long-term sustainability. More fundamentally, the intrinsic incompatibility between non-replicable inorganic materials and self-replicating microbial cells imposes a hard constraint on the stability, scalability and long-term performance of conventional biohybrid systems. While many alternative materials currently face trade-offs in light absorption and charge separation, continued optimization of

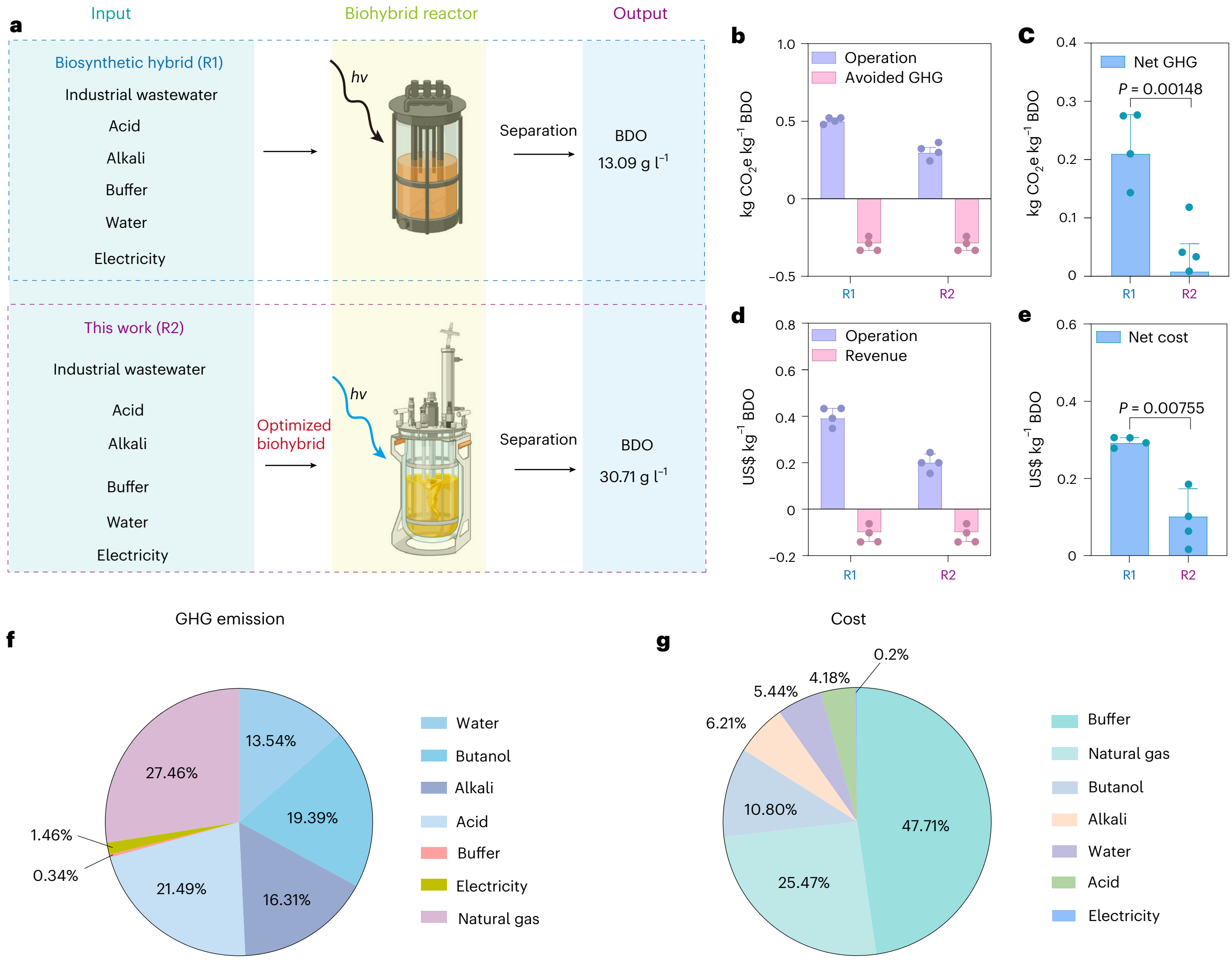

Fig. 6 | LCA. a, A comparative analysis was conducted between previously reported and the present solar-driven biohybrid reactor pathways for BDO production. **b**–**e**, System boundary of the LCA for the wastewater-based, solar-driven biohybrid reactor, and comparison of GHG emissions (**b**,**c**) and economic costs (**d**,**e**) with current production routes and previous studies on solar-driven biohybrid wastewater fermentation. The net GHG emissions (**c**) of BDO (blue) include the positive emissions from the operation of solar-driven biohybrid synthesis (purple) and the avoided emissions (**b**) from industrial wastewater treatment (pink), while the net cost (**e**; blue) benefits from the revenues associated with avoided wastewater treatment and valuable by-products (**d**; pink). Bar charts with error bars and data distributions (the figure presents the maximum, minimum, median and mean values; *n* = 4) were generated based on 10,000 Monte Carlo simulation runs, representing the 10–90% confidence interval. See Methods for details of routes R1 and R2. **f**,**g**, Analysis of GHG emission contributions (**f**) and cost contributions (**g**) in the operation process of the R1 route and R2 route. Each pie chart displays the distribution of different contributing factors, either materials or energy, to the total GHG or cost for each fabrication route. All *P* values are determined by a two-tailed unpaired *t*-test. Icons in **a** created in BioRender; Guo, M. https://biorender.com/7c6h88h (2026).

their properties and biointerfaces may help to narrow this performance gap and enable more robust, sustainable biohybrid platforms.

Methods

Transient absorption measurements

Transient absorption measurements were conducted using a Yb:KGW amplifier (Pharos, Light Conversion) combined with a pump–probe system (HARPIA-TA, Light Conversion). The fundamental laser (1,030 nm, ~190 fs, 89 kHz) from the amplifier was split into two beams. One beam was used to pump an optical parametric amplifier (Orpheus, Light Conversion) and a second harmonic generator (Lyra, Light Conversion) to generate a tunable pump pulse. The other 1,030-nm beam was focused into a sapphire crystal to produce a white light continuum as a probe pulse. The pump and probe pulses were focused and overlapped onto the sample. The transmitted probe pulse was dispersed by a monochromator (Andor Kymera 193i-B2) and detected by a silicon-based array detector. The pump–probe delay can be up to 8 ns controlled by a delay line. The samples are measured in an optical cuvette with a 2-mm optical pathlength. The measured sample with CC NPLs was cocultured for 3 hours. One transient measurement takes about 40 min and involves 6 individual scans. The signal shows no degradation. The transient experiments were done under a continuous blue light (5 mW cm^{-2}) excitation of the XG211 to keep the cell activity.

Construction of biohybrid systems for BDO, PHB and α-farnesene production

The strains XG211, XG256 and XG257 were inoculated in VN medium supplemented with 1.5 mg l^{-1} CdS, and the OD$_{600}$ was adjusted to 0.1 to ensure optimal starting-cell concentration. Aerobic cultivation was carried out in an incubator set at 37 °C to promote bacterial growth under controlled conditions. After 3 hours of cultivation, the cells were collected, washed once with fresh VN medium to remove excess nutrients, and then the OD_{600} was adjusted to approximately 2.0 to standardize the cell density for subsequent experiments. To initiate the reaction, 1 mM cysteine was added as an electron sacrificial agent, and 5 μM FMN was included as an electron mediator to facilitate the electron transfer process. For the evaluation of intracellular electron mediators involved in BDO biosynthesis, 5 μM FMN, 100 μM riboflavin, 100 μM phenazine and 100 μM 1,4-naphthoquinone were individually added to the system. The biohybrid system was then exposed to 5 mW cm^{-2} blue light (470 nm) for 1 hour at 37 °C, with continuous agitation at 200 rpm to ensure even illumination and proper mixing of the components. After the light exposure, the fermentation liquid or cells were collected and analysed for BDO by GC, PHB by high-performance liquid chromatography (HPLC) and α-farnesene by GC–mass spectrometry (GC–MS). The bacterial cells were also harvested for further metabolite analysis to assess intracellular changes and by-products generated during the experiment.

Photoelectrochemical analysis

The ultraviolet–visible (UV–vis) absorption spectra were measured using a Cary 5000 spectrophotometer (Agilent) to determine the direct bandgap of the materials. To prepare the samples, dispersed nanoparticles or semiconductor biohybrids were first loaded onto carbon paper substrates, which served as conductive support. The materials were then uniformly spread over a 1 × 1 cm^2 area by drop casting, followed by vacuum drying to ensure uniform film formation and adhesion to the carbon paper. For photoelectrochemical measurements, a standard three-electrode configuration was used in a phosphate-buffered saline electrolyte. Ag/AgCl (3-M NaCl) was used as the reference electrode, and a platinum (Pt) wire was employed as the counter electrode to complete the electrochemical cell. The photoelectrochemical activity of the films was tested under a 470-nm blue light panel, which was calibrated to provide an intensity of 5 mW cm^{-2} to ensure consistent illumination. Current densities were recorded under a 0.5-V bias versus Ag/AgCl to evaluate the photoelectrochemical performance of the biohybrids. These measurements were taken under controlled illumination conditions to assess their light-driven charge transport properties, which are critical for determining their efficiency in solar energy conversion applications.

Quantifying intracellular metabolites in biohybrids

To quantify intracellular metabolites, the extraction method was adapted from ref. 12. The biohybrids were exposed to 5 mW cm^{-2} of light intensity for 1 hour to stimulate metabolic activity. Following this light exposure, the cells were harvested by centrifugation at 13,000 × *g* for 10 min at 4 °C to pellet the biohybrids. Immediately after centrifugation, the cell pellets were resuspended in 1 ml of pre-cooled methanol/water (80:20, vol/vol) mixture, which was kept at −80 °C to minimize metabolite degradation during extraction. To ensure complete extraction, the samples were centrifuged again at 13,000 × *g* for 10 min at 4 °C, after which the supernatants were carefully collected. These supernatants contained intracellular metabolites, which were then subjected to further analysis using LC–MS/MS. The LC–MS/MS analysis was performed using a SCIEX Triple Qua 5000+ QTRAP Ready mass spectrometer, which provided high sensitivity and specificity for the quantification of a wide range of metabolites.

Quantifying BDO and glucose concentration

To determine the BDO concentration, the bacterial culture was centrifuged at 12,000 × *g* for 10 min, and the same volume of supernatant and isometric ethyl acetate was mixed for sonication for 20 min and centrifuged for 10 min. Supernatant was filtered using nylon membrane (0.22 μm) and then determined using GC. The GC system (Agilent 8890, Agilent Technologies, Inc.) is equipped with a DB-WAX capillary column (30 m × 0.53 mm × 1 μm) and a flame ionization detector. Hydrogen gas was used as the carrier gas. The injector and detector temperature were maintained at 250 °C, and the oven temperature was 80 °C. The injection volume was 1 μl. To obtain the calibration curves for quantifying BDO and acetoin, a series of standards were quantified by the GC system after the same pretreatment. Glucose content was determined using glucose assay reagent (Beyotime).

Quantification of PHB production

The quantification of PHB was performed based on previously reported methods. A 1-ml aliquot of the bacterial culture was collected and washed twice with 1 ml of ice-cold deionized water. The cells were then lysed in 200 μl of methanol and incubated at 60 °C for 30 min to remove methanol. To hydrolyse PHB, 200 μl of 98% sulfuric acid was added to the dried cell pellet, followed by incubation at 37 °C for 2 hours and subsequently at 95 °C for 40 min. The samples were then diluted tenfold with deionized water, filtered through a 0.22-μm membrane filter, and analysed using HPLC equipped with an Aminex HPX-87H column (300 × 7.8 mm, Bio-Rad). The HPLC system used was an Agilent 1260 Infinity series, with a mobile phase of 5-mM H_2SO_4 aqueous solution at a flow rate of 0.7 ml min^{-1}. The column temperature was maintained at 50 °C.

Quantification of α-farnesene production

The dodecane phase of the biphasic culture was collected and centrifuged at 12,000 × *g* for 10 min to remove cellular debris. The resulting supernatant was subsequently analysed using GC–MS to quantify the produced α-farnesene. GC–MS analysis was performed on an Agilent 19091J-433 GC–MS system (Agilent Technologies). Samples were injected with a split ratio of 1:20, and 0.4 μl of each sample was separated using an HP-5ms capillary column (30.0 m × 0.25 mm × 0.25 μm, Agilent Technologies). The oven temperature was initially held at 160 °C for 2 min, then increased at a rate of 15 °C min^{-1} to 205 °C, followed by a post-run period at 280 °C for 5 min. Helium was used as the carrier gas at an inlet pressure of 14 psi. The detector temperature was maintained at 250 °C. A standard curve was constructed using α-farnesene (Aladdin) as the reference compound to estimate the yield of α-farnesene.

Extracellular NADH regeneration assay

In a 1-ml reaction mixture of VN medium containing 1 mM NAD^+, 1.5 mg ml^{-1} of CC NPLs and 1 mM cysteine as a sacrificial agent, the components were carefully mixed to initiate the reaction. The reaction was allowed to proceed for 2 hours under controlled conditions. During this period, the conversion of NAD^+ to NADH was facilitated by the electron transfer from the CC NPLs and the sacrificial agent, cysteine. To quantify the amount of NADH generated, the absorbance at 340 nm was measured using a UV–vis spectrophotometer, as NADH absorbs strongly at this wavelength, and the change in absorbance correlates with NADH production. Additionally, the effect of adding 5 μM FMN or 0.6 mM thiamine or 0.6 mM TPP to the reaction mixture was investigated to determine their impact on NADH production. These compounds were included to evaluate their potential role in enhancing the electron transfer and NADH regeneration processes within the system. For more precise quantification of NADH content, NMR spectroscopy was employed. A 450-μl aliquot of the sample solution was prepared and mixed with 50 μl of D_2O to provide a deuterated solvent for NMR analysis. NMR measurements were performed using either the Bruker AVANCE NEO 400 MHz or the AVANCE III HD50 MHz spectrometer, both of which provide high-resolution spectra for metabolite analysis. The acquired NMR data were processed and analysed using Bruker TopSpin software. This method provided valuable insight into the effect of different additives on the NADH generation process, as well as the efficiency of the biohybrid system in catalysing the conversion of NAD^+ to NADH.

Calculation of quantum efficiency of biohybrids

The calculation methods of quantum efficiency (QE) were mostly applicable to monochromatic or single wavelength light, such as

$$\mathrm{QE}\,\% = \frac{\text{electrons}}{\text{photons}} = \frac{2 \times C_a \times V \times N_A}{\Phi_{ph} \times t \times A} \times 100\,\%$$

where N_A is Avogadro's constant ($6.02 \times 10^{23}\,\mathrm{mol}^{-1}$), and C_a represents the difference in the molar amount of BDO production between biohybrid systems and non-hybrid systems, with the subscript *a* denoting the actual measured value. V is the total suspension volume (1 ml) and Φ_{ph} is the measured average photon flux,

$$\Phi_{ph} = \frac{P\lambda}{hc}.$$

P, λ, h and c denote the incident light power density at a given wavelength ($5\,\mathrm{mW\,cm^{-2}}$), the incident light wavelength (470 nm), Planck's constant ($6.62 \times 10^{-34}\,\mathrm{J{\cdot}s}$) and the speed of light ($3 \times 10^{8}\,\mathrm{m\,s^{-1}}$), respectively. $\Phi_{ph}\,\mathrm{cm^{-2}\,s^{-1}} = 1.18 \times 10^{16}\,\mathrm{cm^{-2}\,s^{-1}}$. t is the reaction time (3,600 s). A is the area of illumination ($1.4\,\mathrm{cm^2}$), calculated by multiplying the vial's outer diameter (1.0 cm) by the height of the cell suspension (1.4 cm).

$$\mathrm{Acetoin} + \mathrm{NADH} + \mathrm{H}^+ \rightarrow \mathrm{BDO} + \mathrm{NAD}^+$$

$$\mathrm{NAD}^+ + 2\mathrm{e}^- + \mathrm{H}^+ \rightarrow \mathrm{NADH}$$

$$\mathrm{Acetoin} + 2\mathrm{e}^- + \mathrm{H}^+ \rightarrow \mathrm{BDO}$$

$$\mathrm{QE_{BDO}}\% = \frac{2 \times 6.02 \times 10^{23} \times 1.4 \times 10^{-6}}{1.18 \times 3.6 \times 1.4 \times 10^{19}} \times 100\% = 2.83\%$$

$$\mathrm{AcCoA} + \mathrm{NADPH} + \mathrm{H}^+ \rightarrow \mathrm{PHB} + \mathrm{NADP}^+$$

$$\mathrm{NADP}^+ + 2\mathrm{e}^- + \mathrm{H}^+ \rightarrow \mathrm{NADPH}$$

$$\mathrm{AcCoA} + 2\mathrm{e}^- + \mathrm{H}^+ \rightarrow \mathrm{PHB}$$

$$\mathrm{QE_{PHB}}\% = \frac{2 \times 6.02 \times 10^{23} \times 6.49 \times 10^{-7}}{1.18 \times 3.6 \times 3 \times 1.4 \times 10^{19}} \times 100\% = 0.44\%$$

$$\mathrm{HMG-CoA} + 3\mathrm{ATP} + 2\mathrm{NADH} + 2\mathrm{H}^+ \rightarrow \mathrm{Mevalonate} + 3\mathrm{ADP} + 2\mathrm{NAD}^+$$

$$3\mathrm{ATP} = \mathrm{NADH}$$

$$\mathrm{NAD}^+ + 2\mathrm{e}^- + \mathrm{H}^+ \rightarrow \mathrm{NADH}$$

$$\mathrm{HMG-CoA} + 6\mathrm{e}^- + 4\mathrm{H}^+ \rightarrow \mathrm{Mevalonate}$$

$$\mathrm{QE}_{\alpha\text{-farnesene}}\,\% = \frac{6 \times 6.02 \times 10^{23} \times 5.25 \times 10^{-8}}{1.18 \times 3.6 \times 1.4 \times 10^{19}} \times 100\,\% = 0.32\,\%$$

BDO production from various substrates by biohybrids

BDO production by XG211 biohybrids was evaluated using different carbon sources, including mannitol, cellulose, chitosan and industrial wastewater. For mannitol, $20\,\mathrm{g\,l^{-1}}$ of mannitol was added to VN medium, which was then used for XG211 preculture and biohybrid construction. The culture was adjusted to an $\mathrm{OD_{600}}$ of 2.0, supplemented with 1 mM cysteine, 5 µM FMN and 0.6 mM TPP, and exposed to blue light ($5\,\mathrm{mW\,cm^{-2}}$, 470 nm). BDO production was monitored at various time points. The samples were filtered through a 0.22-µm membrane and analysed for mannitol using HPLC equipped with an Aminex HPX-87H column (300 × 7.8 mm, Bio-Rad) on an Agilent 1260 Infinity system. The mobile phase consisted of 5 mM $\mathrm{H_2SO_4}$ at a flow rate of $0.8\,\mathrm{ml\,min^{-1}}$, with the column temperature maintained at 60 °C.

For cellulose, $20\,\mathrm{g\,l^{-1}}$ was hydrolysed with $30\,\mathrm{FPU\,g^{-1}}$ of cellulase in a buffer solution (pH 4.8) at 50 °C. After 48 hours, the hydrolysate was centrifuged, and the supernatant was heated at 100 °C to inactivate residual enzymes and remove unreacted cellulose. VN medium salts were then added to the supernatant at the appropriate ratio, and the pH was adjusted to 7.5. This medium was used for preculturing strain XG211 and constructing the biohybrid system. The culture was adjusted to an $\mathrm{OD_{600}}$ of 2.0, supplemented with 1 mM cysteine, 5 µM FMN and 0.6 mM TPP, and incubated under blue light irradiation ($5\,\mathrm{mW\,cm^{-2}}$, 470 nm). Samples were collected at different time points to determine BDO production. Residual sugars were quantified using the anthrone–sulfuric acid method.

For chitosan, $20\,\mathrm{g\,l^{-1}}$ was hydrolysed with $30\,\mathrm{U\,ml^{-1}}$ of chitosanase in a buffer solution (pH 5.0) at 45 °C for 2 hours. After hydrolysis, the mixture was centrifuged, and the supernatant was heated at 100 °C to remove residual enzymes and undigested chitosan. VN medium salts were added to the hydrolysate at the appropriate ratio, and the pH was adjusted to 7.5. This medium was then used for XG211 preculture and biohybrid construction. The culture was adjusted to an $\mathrm{OD_{600}}$ of 2.0, supplemented with 1 mM cysteine, 5 µM FMN and 0.6 mM TPP, and exposed to blue light ($5\,\mathrm{mW\,cm^{-2}}$, 470 nm). BDO production was measured at various time intervals.

For industrial wastewater, molasses wastewater was diluted to a final sugar concentration of $50\,\mathrm{g\,l^{-1}}$ and used to prepare VN medium. The resulting medium was used for bacterial culture and biohybrid assembly. The culture was adjusted to an $\mathrm{OD_{600}}$ of 2.0, supplemented with 1 mM cysteine, 5 µM FMN and 0.6 mM TPP, and irradiated with blue light ($5\,\mathrm{mW\,cm^{-2}}$, 470 nm). Samples were taken at different time points to assess BDO production.

Scalable BDO production from wastewater by biohybrids

To evaluate the scalability of BDO production using biohybrids, bacteria were initially cultured in rich medium until $\mathrm{OD_{600}} \approx 1.0$. The culture was then inoculated at 2% (vol/vol) into VN medium containing $4\,\mathrm{g\,l^{-1}}$ molasses wastewater and supplemented with $1.5\,\mathrm{mg\,l^{-1}}$ CC NPLs. When the culture reached $\mathrm{OD_{600}} \approx 1.0$ again, cells were harvested and resuspended to $\mathrm{OD_{600}} \approx 2.0$, then transferred into a 5-l bioreactor containing 3 l of VN medium with $50\,\mathrm{g\,l^{-1}}$ molasses as the carbon source. Additionally, 1 mM cysteine, 5 µM FMN and 0.6 mM TPP were supplemented. The fed-batch fermentation was performed as a single run, in which an additional $30\,\mathrm{g\,l^{-1}}$ molasses was added every 12 hours. The culture was exposed to 470 nm blue light at an intensity of $5\,\mathrm{mW\,cm^{-2}}$. Fermentation was conducted at 37 °C with pH maintained at 7.0, and an aeration rate of 500 ccm. Samples were collected at different time points for the quantification of BDO and total sugar content, the latter determined using the anthrone–sulfuric acid method.

LCA

Following the approach of Pi et al.[12], the primary goal of this study was to comprehensively evaluate the environmental and economic performance of BDO production via our wastewater-based, solar-driven biohybrid synthesis (Case R2) and compare the work of Pi et al.[12] (Case R1). The functional unit was defined as the production of 1 kg of BDO. The system boundary adopted a 'cradle-to-gate' approach, encompassing all processes, from raw material extraction and transportation to the final BDO product at the factory gate. This includes feedstock acquisition (wastewater collection), energy inputs (electricity for solar-driven processes and water), chemical production, and the BDO synthesis and separation stages.

For life-cycle inventory, foreground process data for the wastewater-based biohybrid synthesis (Case R1), including specific material and energy consumption rates per functional unit, were directly adapted from the experimental results reported by Pi et al.[12]. The foreground inventory of Case R1 was calculated for Case R2 by applying the methodological framework and stoichiometric models also established by Pi et al.[12]. This approach ensures that the technological assumptions for both cases are consistent and comparable. The background data for all processes, such as the production of chemicals, electricity grid mix and transportation, were sourced from the ecoinvent 3.6 database, using 'Rest-of-World' (RoW) or 'Global' (GLO) datasets to represent average market conditions. Detailed life-cycle inventories for all cases are provided in Supplementary Table 11.

Environmental impacts were evaluated using SimaPro v9.X to perform life-cycle impact assessment. For climate change, we used the IPCC 2021 GWP100a method to quantify GHG emissions in kg CO_2e. Other environmental impacts, such as terrestrial acidification and human toxicity, were evaluated using the ReCiPe 2016 Midpoint (H) method. The total environmental impact (EI) for each category was calculated using the following equation:

$$\mathrm{EI}_i = \sum_{j=1}^{n} (\mathrm{CA}_j \times \mathrm{EF}_j)$$

EI_i represents the environmental impact of process i, which includes the production of 1 kg of BDO via fossil fuel refining, sugar fermentation and wastewater-based biohybrid synthesis. CA_j denotes the consumption of input j (for example, materials, chemicals, energy) for BDO production, while EF_j refers to the environmental factor associated with input j, as determined using IPCC 2021 GWP100 or ReCiPe 2016 Midpoint (H). Environmental impacts and GHG emissions via synthesized biohybrid using wastewater are provided in Supplementary Tables 9 and 12. To account for GHG emissions volatility and uncertainty in the Case R2, a Monte Carlo simulation with 10,000 iterations was performed. This simulation generated a distribution of potential GHG emissions, from which the maximum, minimum, mean and median values were derived (Supplementary Table 9). The mean cost value was used for the primary comparison in this study.

An economic assessment was conducted in parallel with the LCA, sharing the same functional unit and system boundary of the work of Pi et al.[12]. The analysis was based on a cost model, calculating the total production cost from the direct costs of raw materials, chemicals and utilities. The unit prices for all inputs were the same as the work of Pi et al.[12], with all costs normalized to US dollars. The detailed cost breakdown is provided in Supplementary Table 11. To account for price volatility and uncertainty in the economic data, a Monte Carlo simulation with 10,000 iterations was performed. Price inputs were modelled using triangular distributions with defined minimum, maximum and most likely values. This simulation generated a distribution of potential production costs, from which the maximum, minimum, mean and median values were derived (Supplementary Table 10). The mean cost value was used for the primary comparison in this study.

LCA was used to quantify the environmental and cost benefits of the solar-driven biohybrid synthesis technology that eliminates the wastewater treatment step. The molasses wastewater (high chemical oxygen demand) and electroplating wastewater (heavy-metal laden) treated here match the type and process chain reported by Pi et al.[12]. Their operation-phase data are therefore adopted directly. The main line is an anaerobic–anoxic–aerobic process with primary pretreatment; tertiary treatment applies coagulation–flocculation, sedimentation, filtration and UV reduction. The functional unit is 1 m^3 of inlet wastewater; excess sludge is thickened, dewatered and landfilled. Construction and demolition impacts are negligible compared with those of the operation phase, during which electricity and chemicals account for ~90 % of environmental load. Only this phase is considered; the resulting GHG offsets and cost savings are listed in Supplementary Tables 9 and 10.

Reporting summary

Further information on research design is available in the Nature Portfolio Reporting Summary linked to this article.

Data availability

The data supporting the findings of this study are available within the article and its Supplementary Information. The RNA-seq data generated in this study have been deposited in the NCBI SRA database under bioproject accession number PRJNA1412514. Other data that support the findings of this study are available from the corresponding authors upon reasonable request. Source data are provided with this paper.

References

1. Lee, W. H. et al. Floatable photocatalytic hydrogel nanocomposites for large-scale solar hydrogen production. *Nat. Nanotechnol.* **18**, 754–762 (2023).
2. Ye, J. et al. Solar-driven methanogenesis with ultrahigh selectivity by turning down H_2 production at biotic–abiotic interface. *Nat. Commun.* **13**, 6612 (2022).
3. Sakimoto, K. K., Wong, A. B. & Yang, P. Self-photosensitization of nonphotosynthetic bacteria for solar-to-chemical production. *Science* **351**, 74–77 (2016).
4. Yu, W. et al. Solar-powered multi-organism symbiont mimic system for beyond natural synthesis of polypeptides from CO_2 and N_2. *Sci. Adv.* **9**, eadf6772 (2023).
5. Wu, D., Zhang, W., Fu, B. & Zhang, Z. Living intracellular inorganic–microorganism biohybrid system for efficient solar hydrogen generation. *Joule* **6**, 2293–2303 (2022).
6. Li, H. et al. Membraneless organelles assembled by AuNPs-enzyme integration in non-photosynthetic bacteria: achieving high specificity and selectivity for solar hydrogen production. *Chem. Eng. J.* **492**, 152207 (2024).
7. Keasling, J. D. Manufacturing molecules through metabolic engineering. *Science* **330**, 1355–1358 (2010).
8. Guo, L. et al. Engineering *Escherichia coli* lifespan for enhancing chemical production. *Nat. Catal.* **3**, 307–318 (2020).
9. Choi, K. R. & Lee, S. Y. Systems metabolic engineering of microorganisms for food and cosmetics production. *Nat. Rev. Bioeng.* **1**, 832–857 (2023).
10. Scown, C. D. & Keasling, J. D. Sustainable manufacturing with synthetic biology. *Nat. Biotechnol.* **40**, 304–307 (2022).
11. Guo, J. et al. Light-driven fine chemical production in yeast biohybrids. *Science* **362**, 813–816 (2018).
12. Pi, S. et al. Solar-driven waste-to-chemical conversion by wastewater-derived semiconductor biohybrids. *Nat. Sustain.* **6**, 1673–1684 (2023).
13. Xiao, K. et al. Interfacing iodine-doped hydrothermally carbonized carbon with *Escherichia coli* through an 'add-on' mode for enhanced light-driven hydrogen production. *Energy Environ. Sci.* **11**, 2100291 (2021).
14. Zheng, T. et al. Upcycling CO_2 into energy-rich long-chain compounds via electrochemical and metabolic engineering. *Nat. Catal.* **5**, 388–396 (2022).
15. Liang, J. et al. Revisiting solar energy flow in nanomaterial–microorganism hybrid systems. *Chem. Rev.* **124**, 9081–9112 (2024).
16. Voiry, D., Shin, H. S., Loh, K. P. & Chhowalla, M. Low-dimensional catalysts for hydrogen evolution and CO_2 reduction. *Nat. Rev. Chem.* **2**, 0105 (2018).

17. Wang, Q., Kalathil, S., Pornrungroj, C., Sahm, C. D. & Reisner, E. Bacteria–photocatalyst sheet for sustainable carbon dioxide utilization. *Nat. Catal.* **5**, 633–641 (2022).
18. Han, H. X. et al. Reversing electron transfer chain for light-driven hydrogen production in biotic–abiotic hybrid systems. *J. Am. Chem. Soc.* **144**, 6434–6441 (2022).
19. Kornienko, N. et al. Spectroscopic elucidation of energy transfer in hybrid inorganic–biological organisms for solar-to-chemical production. *Proc. Natl. Acad. Sci. USA* **113**, 11750–11755 (2016).
20. Okoro, G. et al. Emerging trends in nanomaterials for photosynthetic biohybrid systems. *ACS Macro. Lett.* **5**, 95–115 (2023).
21. Lin, Y. et al. Periplasmic biomineralization for semi-artificial photosynthesis. *Sci. Adv.* **9**, eadg5858 (2023).
22. Kim, G. M. et al. In vivo synthesis of semiconductor nanoparticles in *Azotobacter vinelandii* for light-driven ammonia production. *Nanoscale* **17**, 3381–3388 (2025).
23. Fang, H. & Hu, W. Photogating in low dimensional photodetectors. *Adv. Sci.* **4**, 1700323 (2017).
24. Lu, Q. et al. Low-dimensional-materials-based flexible artificial synapse: materials, devices, and systems. *Nanomaterials* **13**, 373 (2023).
25. Shaw, Z. L. et al. Antipathogenic properties and applications of low-dimensional materials. *Nat. Commun.* **12**, 3897 (2021).
26. Li, Y. et al. Graphene microsheets enter cells through spontaneous membrane penetration at edge asperities and corner sites. *Proc. Natl. Acad. Sci. USA* **110**, 12295–12300 (2013).
27. Diroll, B. T. et al. 2D II–VI semiconductor nanoplatelets: from material synthesis to optoelectronic integration. *Chem. Rev.* **123**, 3543–3624 (2023).
28. Hu, Z., O'Neill, R., Lesyuk, R. & Klinke, C. Colloidal two-dimensional metal chalcogenides: realization and application of the structural anisotropy. *Acc. Chem. Res.* **54**, 3792–3803 (2021).
29. Wu, K. & Lian, T. Quantum confined colloidal nanorod heterostructures for solar-to-fuel conversion. *Chem. Soc. Rev.* **45**, 3781–3810 (2016).
30. Alsalme, A. & Alsaeedi, H. Twenty-two percent efficient Pb-free all-perovskite tandem solar cells using SCAPS-1D. *Nanomaterials* **13**, 96 (2022).
31. Xu, Y. et al. Systematic metabolic engineering of *Escherichia coli* for high-yield production of fuel bio-chemical 2,3-butanediol. *Metab. Eng.* **23**, 22–33 (2014).
32. Yang, Y., Liu, L. N., Tian, H., Cooper, A. I. & Sprick, R. S. Making the connections: physical and electric interactions in biohybrid photosynthetic systems. *Energy Environ. Sci.* **16**, 4305–4319 (2023).
33. Liu, Z., Wang, K., Chen, Y., Tan, T. & Nielsen, J. Third-generation biorefineries as the means to produce fuels and chemicals from CO_2. *Nat. Catal.* **3**, 274–288 (2020).
34. Guan, X. et al. Maximizing light-driven CO_2 and N_2 fixation efficiency in quantum dot–bacteria hybrids. *Nat. Catal.* **5**, 1019–1029 (2022).
35. Zhao, C. et al. Metabolite cross-feeding promoting NADH production and electron transfer during efficient SMX biodegradation by a denitrifier and *S. oneidensis* MR-1 in the poresence of nitrate. *Environ. Sci. Technol.* **57**, 18306–18316 (2023).
36. Lin, J.-H., Lee, M.-C., Sue, Y.-S., Liu, Y.-C. & Li, S.-Y. Cloning of *phaCAB* genes from thermophilic *Caldimonas manganoxidans* in *Escherichia coli* for poly(3-hydroxybutyrate) (PHB) production. *Appl. Microbiol. Biotechnol.* **101**, 6419–6430 (2017).
37. Liu, Y. et al. Engineering the oleaginous yeast *Yarrowia lipolytica* for production of α-farnesene. *Biotechnol. Biofuels* **12**, 296 (2019).
38. Anthony, J. R. et al. Optimization of the mevalonate-based isoprenoid biosynthetic pathway in *Escherichia coli* for production of the anti-malarial drug precursor amorpha-4,11-diene. *Metab. Eng.* **11**, 13–19 (2009).
39. Yadav, I., Rautela, A., Rawat, S., Namdeo, A. K. & Kumar, S. in *Advances in Yeast Biotechnology for Biofuels and Sustainability* (eds Daverey, A. et al.) 73–97 (Elsevier, 2023).
40. Ji, W. et al. Nanomaterial–biological hybrid systems: advancements in solar-driven CO_2-to-chemical conversion. *Green Carbon* **2**, 322–336 (2024).

Acknowledgements

We extend our gratitude to P. Xu's group for their generous provision of the pET28a-*RABC* vector containing BDO biosynthetic genes. We sincerely thank X. Liu's group for generously providing the biosynthetic genes *SoNar* and *iNap1*. We acknowledge the Shenzhen Synthetic Biology Infrastructure for instrument support and technical assistance. This work was supported by the National Natural Science Foundation of China (grant nos 32230060, 32522056, 32171426, 31925001, 22171132, 52200090, 52300181), the Science and Technology Program in Jiangsu province (BK20232041), the National Key R&D Program of China (grant nos 2021YFA0910800, 2021YFA0909900, 2022YFC3401802, 2024YFB4105700), Shenzhen Science and Technology Program (grant nos JCYJ20220818101804010, RCYX20221008092901004, ZDSYS20220606100606013, KJZD20230923114419039 and JCYJ20220531100006011), Shanghai Municipal Science and Technology Major Project, the Guangdong Basic and Applied Basic Research Foundation (2024B1515020102), the Program for Innovative Talents and Entrepreneurs in Jiangsu (020513006012 and 020513006014) and the Zijin Scholars Foundation (0205181022), NUS Start-up Fund and the MOE AcRF Tier 1 Grant (project no. WBS A-8001945-00-00).

Author contributions

The project was conceptualized by Y.W. and X.G., and was supervised by C.Y., X.G., Y.W. and Y.L. X.K. prepared the materials and performed the characterization. M.G. performed the experiments of the biohybrid construction and characterization. W.C. and H.L. performed the metabolomics. W.Y. and Y.X. performed the experiment of CRISPRi. H.X. performed flux balance analysis. S.P. performed the experiment of photocurrent measurement. X.W. conducted LCA analysis. R.M. performed computational analysis simulating the entry of nanomaterials into cells. M.G., X.K., Y.W. and X.G. wrote the paper with input from all authors. All authors discussed the results and commented on the paper.

Competing interests

The authors declare no competing interests.

Additional information

Supplementary information The online version contains supplementary material available at https://doi.org/10.1038/s41893-026-01787-x.

Correspondence and requests for materials should be addressed to Chen Yang, Yuanyuan Wang or Xiang Gao.

Peer review information *Nature Sustainability* thanks Zhi Cao, Sai Kishore Ravi and the other, anonymous, reviewer(s) for their contribution to the peer review of this work.

---

[1]State Key Laboratory of Quantitative Synthetic Biology, Shenzhen Institute of Synthetic Biology, Shenzhen Institutes of Advanced Technology, Chinese Academy of Sciences, Shenzhen, China. [2]University of Chinese Academy of Sciences, Beijing, P. R. China. [3]State Key Laboratory of Coordination Chemistry, School of Chemistry and Chemical Engineering, Nanjing University, Nanjing, China. [4]CAS-Key Laboratory of Synthetic Biology, Key Laboratory of Plant Carbon Capture, CAS Center for Excellence in Molecular Plant Sciences, Shanghai Institute of Plant Physiology and Ecology, Chinese Academy of Sciences, Shanghai, China. [5]State Key Laboratory of Microbial Metabolism, and School of Life Sciences and Biotechnology, Shanghai Jiao Tong University, Shanghai, China. [6]Faculty of Synthetic Biology, Shenzhen University of Advanced Technology, Shenzhen, P. R. China. [7]Department of Physics, College of Physical Science and Technology, Xiamen University, Xiamen, China. [8]Department of Chemical and Biomolecular Engineering, National University of Singapore, Singapore, Singapore. [9]These authors contributed equally: Mingming Guo, Xinke Kong. ✉e-mail: yang.c@sjtu.edu.cn; wangyy@nju.edu.cn; gaoxiang@siat.ac.cn

nature portfolio

Corresponding author(s): Xiang Gao; Yuanyuan Wang; Chen Yang

Last updated by author(s): Jan 25,2026

Reporting Summary

Nature Portfolio wishes to improve the reproducibility of the work that we publish. This form provides structure for consistency and transparency in reporting. For further information on Nature Portfolio policies, see our Editorial Policies and the Editorial Policy Checklist.

Statistics

For all statistical analyses, confirm that the following items are present in the figure legend, table legend, main text, or Methods section.

n/a	Confirmed	
☐	☒	The exact sample size (*n*) for each experimental group/condition, given as a discrete number and unit of measurement
☐	☒	A statement on whether measurements were taken from distinct samples or whether the same sample was measured repeatedly
☐	☒	The statistical test(s) used AND whether they are one- or two-sided *Only common tests should be described solely by name; describe more complex techniques in the Methods section.*
☒	☐	A description of all covariates tested
☒	☐	A description of any assumptions or corrections, such as tests of normality and adjustment for multiple comparisons
☐	☒	A full description of the statistical parameters including central tendency (e.g. means) or other basic estimates (e.g. regression coefficient) AND variation (e.g. standard deviation) or associated estimates of uncertainty (e.g. confidence intervals)
☐	☒	For null hypothesis testing, the test statistic (e.g. *F*, *t*, *r*) with confidence intervals, effect sizes, degrees of freedom and *P* value noted *Give P values as exact values whenever suitable.*
☒	☐	For Bayesian analysis, information on the choice of priors and Markov chain Monte Carlo settings
☒	☐	For hierarchical and complex designs, identification of the appropriate level for tests and full reporting of outcomes
☒	☐	Estimates of effect sizes (e.g. Cohen's *d*, Pearson's *r*), indicating how they were calculated

Our web collection on statistics for biologists contains articles on many of the points above.

Software and code

Policy information about availability of computer code

Data collection	Intracellular metabolites data were collected using SCIEX OS-MQ 2.0 and Exactive Series Tune 2.8 (Thermo). Nanocrystals characteristion were collected using Carry 5000 (Agilent), HORIBA FL-3 3D fluorescence spectrometer, laser confocal Raman spectrometer (Renishaw InviA-Reflex), JEOL JEM-2800, Bruker D8 Advance diffractometer.
Data analysis	Intracellular metabolites data were analyzed using Analyst 1.7, Thermo Scientific Xcalibur 4.2.47, and Thermo Compound Discoverer 2.0. GraphPad Prism (v 9.0) was used for most data analysis. MDI jade 6 and avantage were used for materials analysis. iLC858_v1.1 and COBRApy were used for Flux Balance Analysis.

For manuscripts utilizing custom algorithms or software that are central to the research but not yet described in published literature, software must be made available to editors and reviewers. We strongly encourage code deposition in a community repository (e.g. GitHub). See the Nature Portfolio guidelines for submitting code & software for further information.

Data

Policy information about availability of data

All manuscripts must include a data availability statement. This statement should provide the following information, where applicable:

- Accession codes, unique identifiers, or web links for publicly available datasets
- A description of any restrictions on data availability
- For clinical datasets or third party data, please ensure that the statement adheres to our policy

Data Availability Statement: The authors declare that the data supporting this work are available in the paper, supplementary information files and the source data.

Research involving human participants, their data, or biological material

Policy information about studies with human participants or human data. See also policy information about sex, gender (identity/presentation), and sexual orientation and race, ethnicity and racism.

Reporting on sex and gender	NA
Reporting on race, ethnicity, or other socially relevant groupings	NA
Population characteristics	NA
Recruitment	NA
Ethics oversight	NA

Note that full information on the approval of the study protocol must also be provided in the manuscript.

Field-specific reporting

Please select the one below that is the best fit for your research. If you are not sure, read the appropriate sections before making your selection.

☒ Life sciences ☐ Behavioural & social sciences ☐ Ecological, evolutionary & environmental sciences

For a reference copy of the document with all sections, see nature.com/documents/nr-reporting-summary-flat.pdf

Life sciences study design

All studies must disclose on these points even when the disclosure is negative.

Sample size	Sample size was determined based on extensive laboratory experience and literature in the field, such as the reference doi.org/10.1038/s41893-023-01233-2
Data exclusions	No data excluded for statistical analyses. Representative images were shown in the manuscripts; similar results from experimental repeats were not shown.
Replication	The number of biological replicates we aimed for was at least three with technical replicates in each group. All the experiments were performed independently and reliably reproduced weekly. Fermenter data at different time intervals were collected from one batch, and all attempts at replication were successful. Representative results in one batch were provided in the manuscripts; similar results from experimental repeats were not shown.
Randomization	Experimental groups were formed based on what was being tested with random sections.
Blinding	Experiments were blinded during imaging, metabolites measuring, and the investigators were blinded to group allocation. All data were analyzed by multiple authors and reviewed by the corresponding authors.

Reporting for specific materials, systems and methods

We require information from authors about some types of materials, experimental systems and methods used in many studies. Here, indicate whether each material, system or method listed is relevant to your study. If you are not sure if a list item applies to your research, read the appropriate section before selecting a response.

Materials & experimental systems

n/a	Involved in the study
☒	☐ Antibodies
☒	☐ Eukaryotic cell lines
☒	☐ Palaeontology and archaeology
☒	☐ Animals and other organisms
☒	☐ Clinical data
☒	☐ Dual use research of concern
☒	☐ Plants

Methods

n/a	Involved in the study
☒	☐ ChIP-seq
☒	☐ Flow cytometry
☒	☐ MRI-based neuroimaging

Plants

Seed stocks	NA
Novel plant genotypes	NA
Authentication	NA